A Model for the Tropical Cyclone Wind Field Response to Idealized Landfall

Jie Chen[a,b] and Daniel R. Chavas[b]

[a] Program in Atmospheric and Oceanic Sciences, Princeton University, Princeton, New Jersey
[b] Department of Earth, Atmospheric and Planetary Sciences, Purdue University, West Lafayette, Indiana

(Manuscript received 15 July 2022, in final form 22 November 2022)

ABSTRACT: The impacts of a tropical cyclone after landfall depend not only on storm intensity but also on the size and structure of the wind field. Hence, a simple predictive model for the wind field after landfall has significant potential value. This work tests existing theory for wind structure and size over the ocean against idealized axisymmetric landfall experiments in which the surface beneath a mature storm is instantaneously dried and roughened individually or simultaneously. Structure theory captures the response of the low-level wind field to different types of idealized landfalls, given the intensity and size response. Storm size, modeled to follow the ratio of simulated time-dependent storm intensity to the Coriolis parameter $v_m(\tau)/f$, can generally predict the transient response of the storm gale wind radii $r_{34\mathrm{kt}}$ to inland surface forcings, particularly for at least moderate surface roughening regardless of the level of drying. Given knowledge of the intensity evolution, the above results combine to yield a theoretical model that can predict the full tangential wind field response to idealized landfalls.

SIGNIFICANCE STATEMENT: A theoretical model that can predict the time-dependent wind field structure of landfalling tropical cyclones (TCs) with a small number of physical, observable input parameters is essential for mitigating hazards and allocating public resources. This work provides a first-order prediction of storm size and structure after landfall, which can be combined with existing intensity predictions to form a simple model describing the inland wind field evolution. Results show its potential utility for modeling idealized inland TC wind fields.

KEYWORDS: Hurricanes/typhoons; Tropical cyclones; Idealized models; Risk assessment

1. Introduction

Predicting the inland impacts of a tropical cyclone (TC) depends not only on the evolution of storm intensity (maximum wind speed) but also on the size and structure of the wind field. Empirical models for TC damage that only depend on intensity while neglecting storm size (Mendelsohn et al. 2012) significantly underestimate losses (Zhai and Jiang 2014). Storm size is known to vary nearly independently of intensity over the ocean (Frank 1977; Merrill 1984; Chavas et al. 2016; Chavas and Lin 2016) and hence predicting the inland impacts requires a model for storm size and structure separate from the intensity. In addition to the direct wind impact, the magnitude and spatial distribution of TC-induced storm surge and heavy rainfall are also strongly dependent on the wind field structure and size (Irish et al. 2008; Lu et al. 2018). Larger TCs may also produce more TC tornadoes away from the TC center (Paredes and Schenkel 2020). Accurate estimation of the postlandfall TC wind field, including structure and size, can help prepare for TC hazards and economic losses.

However, our understanding of the postlandfall evolution of the TC wind field has been limited by insufficient observations and the complexity of landfall processes. The heterogeneity of the inland surface and environmental conditions in the vicinity of the coastline make it difficult to generalize the physics explaining the response of the TC wind field. Recently, Chen and Chavas (2020, hereafter CC20) simplified landfall as a transient response of a mature axisymmetric TC to instantaneous surface roughening or drying and explained how each surface forcing weakens the storm via different mechanistic pathways using idealized numerical simulation experiments. This work complements idealized 3D landfall experiments that identified important asymmetries in the wind field generated by the onshore flow transition from ocean to land (Hlywiak and Nolan 2021, 2022). Chen and Chavas (2021, hereafter CC21) generalized this modeling approach to any combination of surface drying and roughening applied simultaneously to test the existing intensification theory of Emanuel (2012) reformulated to predict intensity decay after landfall. They showed that this solution could predict the intensity decay evolution across experiments, and it also compared well with the prevailing empirical intensity decay model. Moreover, they demonstrated that the intensity response to simultaneous drying and roughening could be modeled as the product of the intensity responses to each forcing individually.

Simple theory for the size and structure of the wind field after landfall has yet to be tested, though. Physical understanding of TC size and structure over the open ocean has advanced significantly in recent decades. Early analytical models proposed an azimuthal wind profile that depends on TC intensity,

---

Denotes content that is immediately available upon publication as open access.

Supplemental information related to this paper is available at the Journals Online website: https://doi.org/10.1175/JAS-D-22-0156.s1.

Corresponding author: Jie Chen, chenjie@princeton.edu

DOI: 10.1175/JAS-D-22-0156.1

© 2023 American Meteorological Society. For information regarding reuse of this content and general copyright information, consult the AMS Copyright Policy (www.ametsoc.org/PUBSReuseLicenses).

Unauthenticated | Downloaded 07/11/23 03:06 AM UTC

radius of maximum wind, and the width of the wind maximum (Holland 1980), which have been tested against observations (Shea and Gray 1973; Willoughby and Rahn 2004). Most recently, the theoretical solutions introduced in Emanuel (2004, hereafter E04) and Emanuel and Rotunno (2011, hereafter ER11) can describe the TC low-level wind field in the convection-free outer region and the convective inner region, respectively. For the convective inner region, ER11 links the radial variation of the outflow temperature to the radial variation of absolute angular momentum beyond radius of maximum wind via the stratification of the outflow driven by small-scale turbulence. For the convection-free outer region, E04 links the radial gradient of absolute angular momentum to the free troposphere subsidence rate W_{cool}, whose value constrained by the heat balance of the free troposphere, via the Ekman dynamics of the boundary layer flow. These two theories are merged together to produce a model for the complete wind profile in Chavas et al. (2015, hereafter C15). The solution takes only a limited number of physical input parameters related to TC intensity, size, latitude, and environmental conditions. This structural model was shown to compare well against observations of the TC wind field and to reproduce the principal modes of wind field variability over the ocean (Chavas and Lin 2016).

TC outer size can vary widely in nature, with size varying more strongly across storms than during the storm life cycle (Chavas and Emanuel 2010; Chavas et al. 2016). The size of a given storm tends to depend strongly on the size of its initiating disturbance, with size often growing slowly with time thereafter (Rotunno and Emanuel 1987; Martinez et al. 2020; Xu and Wang 2010). On the f plane over an ocean surface, TC size expands toward an equilibrium size that scales with the ratio of the potential intensity to the Coriolis parameter, V_p/f (D. Wang et al. 2022; Frisius et al. 2013; Chavas and Emanuel 2014), though slightly different velocity scales have been proposed as well (Khairoutdinov and Emanuel 2013; Zhou et al. 2014, 2017; Emanuel 2022). Recent work has shown that, on the spherical Earth, TC size is set by the Rhines scale, which depends inversely on the square root of the planetary vorticity gradient β (Chavas and Reed 2019). This scaling arises because the TC equilibrium size is much larger than the Rhines scale over the low latitude oceans. Hence, β strongly inhibits storms from expanding to their equilibrium size due to Rossby wave radiation (Lu and Chavas 2022). This framework has yet to be considered in the context of landfall, though. Landfall is characterized by a sharp transition to near-zero V_p and thus near-zero equilibrium size (CC21). At the same time, the Rhines scale would also decrease moderately depending on the storm decay and the northward latitudinal change. With equilibrium size now much smaller than the Rhines scale, TC size would be expected to shrink toward its equilibrium size after landfall, and its dynamics governed by the length scale V_p/f. We explore this avenue below.

Here we examine how existing theory can be used to model the full TC wind field following landfall. This work tests TC size and structure theory against different sets of idealized landfalling storms as in CC21. For structure, we test the theory of C15. For size, we test a simple hypothesis for TC size based on the length scale v_m/f, where the time-dependent intensity v_m is used in place of V_p to allow for a transient response to an instantaneous change in V_p. We seek to answer the following research questions:

1) How well does the C15 wind field model predict the transient response of the azimuthal wind profile to idealized landfall, characterized by instantaneous surface drying and/or roughening?
2) Can the length scale v_m/f predict the transient response of storm outer size?
3) How well is the size response to combined drying and roughening predicted by the product of the responses to each forcing individually, similar to intensity as found in CC21?
4) Can we predict the complete wind field evolution following idealized landfall by combining the structure and size models examined in this work?

This paper is structured as follows. Section 2 reviews the relevant theories. Section 3 describes model setup and reviews relevant existing theory. Section 4 presents our results addressing the research questions. Section 5 summarizes key results, limitations, and the follow-up work.

2. Theory

a. TC wind structure model

Absolute angular momentum is widely applied to understand the physics of the TC wind field, as it is directly linked to the tangential wind speed (Anthes 1974; Montgomery et al. 2001; E04; Lilly and Emanuel 1985). Within the boundary layer, absolute angular momentum transported inward from some outer radius via radial inflow is gradually lost to surface frictional dissipation. That which remains is gradually converted from planetary to relative angular momentum, thereby generating the tangential wind field of the TC vortex. When reaching the radius of maximum wind speed (r_m), air ascends within the convective eyewall and then flows radially outward aloft near the tropopause. Therefore, a theoretical model describing the low-level circulation beyond r_m can be formulated by precisely quantifying how absolute angular momentum changes with radius based on the local dynamics or thermodynamics. Recent work achieves this in two distinct regions: the outer nonconvecting region (E04) and the inner convecting region (ER11).

For the convective inner region, ER11 posits that small-scale shear-induced turbulence stratifies the outflow to a critical Richardson number Ri_c, which for a slantwise neutral vortex translates the stratification of the outflow dT/dz to an increase in outflow temperature T_0 with radius beyond r_m. As a result, the tangential wind speed decreases with radius. The ER11 solution for the radial distribution of M is given by

$$\left(\frac{M_{\mathrm{ER11}}}{M_m}\right)^{2-C_k/C_d} = \frac{2\left(\dfrac{r}{r_m}\right)^2}{2-\dfrac{C_k}{C_d}+\left(\dfrac{C_k}{C_d}\right)\left(\dfrac{r}{r_m}\right)^2}, \qquad (1)$$

where

Unauthenticated | Downloaded 07/11/23 03:06 AM UTC

$$M_m = r_m V_m + \frac{1}{2} f r_m^2 \tag{2}$$

is the angular momentum at r_m, and C_k and C_d are the exchange coefficients of enthalpy and momentum, respectively. With input metrics (v_m, r_m) and the value of C_k and C_d, Eqs. (1) and (2) can generate a complete azimuthal wind profile, though the underlying physics discussed above are only valid for the convecting region beyond r_m.

For the convection-free outer region, boundary layer inflow associated with the surface frictional torque induces an Ekman suction through the top of the boundary layer from the free troposphere. To satisfy mass continuity, the magnitude of the free tropospheric subsidence rate $W_{\rm cool}$ must equal the Ekman suction rate $w_{\rm EK}$, $w_{\rm EK} = -W_{\rm cool}$. The Ekman suction rate is given by

$$w_{\rm EK} = -\int_0^h \frac{1}{r}\frac{\partial(ru)}{\partial r}\partial z. \tag{3}$$

Meanwhile, in this steady-state slab boundary layer with a depth of h, the angular momentum budget is given by

$$hu\frac{\partial M}{\partial r} = -C_d|\mathbf{V}|(rV), \tag{4}$$

where $\mathbf{V}$ is the near surface wind velocity and V is the azimuthal component. Equation (3) can be solved by first vertically integrating the slab layer with a depth of h and then radially integrating the layer from r_0 to r assuming $u = 0$ at r_0, where r_0 is the radius of vanishing wind ($r_{v=0}$), representing the overall storm outer size. Combining the result with Eq. (4) to eliminate hu, taking $w_{\rm EK} = -W_{\rm cool}$, and approximating $\mathbf{V}$ by V yields the solution

$$\frac{\partial M_{\rm E04}}{\partial r} = \chi \frac{(rV)^2}{r_0^2 - r^2}, \tag{5}$$

where $\chi = 2C_d/W_{\rm cool}$. This solution links the radial gradient of M to $W_{\rm cool}$, whose value is constrained by the thermodynamics of the free troposphere and can be estimated from the ambient stratification and radiative cooling rate via radiative-subsidence balance. Equation (5) does not have an analytic solution but can be solved numerically to produce a full azimuthal wind profile that extends inwards from r_0 to an arbitrary radius. The model takes r_0 and χ as input parameters.

C15 mathematically merged the ER11 [Eqs. (1) and (2)] and E04 [Eq. (5)] solutions to produce a model for the complete azimuthal wind profile. This merging yields a unique solution; the process is described in C15. Parameters required to solve the solutions are V_m and r_m for the inner region, V_a and r_a at the merge point connecting the inner and outer region, $r_{\rm fit}$ as a specified radius input, χ and f for the environmental conditions. Given the environmental parameters χ, f, and C_k/C_d, one only needs to know two storm parameters—the intensity V_m and any wind radius (e.g., r_m, $r_{\rm 34kt}$)—to specify the model solution.

C15 is the simplest model that generates a first-order prediction of the full wind field. C15 evaluated the model against real-world storms over the ocean, and the model has been applied in storm surge risk analysis (Xi et al. 2020; Lin et al. 2020; Xi and Lin 2022). In addition, it performs best among existing wind models in simulating peak storm surge from historical U.S. landfalls (S. Wang et al. 2022). Thus, the C15 wind field model is examined against the simulated wind field response to idealized landfalls in this paper. A novel version of C15 is applied in this work, where the wind profile within the eye ($r < r_m$) generated by the ER11 solution is replaced with a quadratic profile as was done in Klotzbach et al. (2022).

b. *TC size*

As described in section 1, TC size on the f plane typically expands toward an equilibrium potential size given approximately by the ratio of the potential intensity to the Coriolis parameter, V_p/f. The size of real-world TCs is typically significantly smaller than this length scale (Chavas and Lin 2016; Chavas and Reed 2019), though, and instead follows the Rhines scale because the latter is much smaller than V_p/f at low latitudes (Chavas and Reed 2019; Lu and Chavas 2022). In contrast, at high latitudes, the potential size is much smaller than the Rhines scale, and hence, the effect of the Rhines scale becomes negligible, yielding a polar cap regime in aquaplanet experiments in which the domain is filled with TCs, analogous to that found on the f plane (Chavas and Reed 2019).

Here we propose an analogous regime contrast for landfall: the transition from ocean to land is a transition to a near-zero value of V_p (CC21) and thus a transition to a regime where V_p/f is suddenly much smaller than the Rhines scale. As with the polar cap regime, the Rhines scale becomes secondary and the TC would be expected to *shrink* toward its potential size, which is near zero. We currently lack an explicit theory for the rate of change of size toward its potential size, though. Instead, we posit that these dynamics ought to depend on V_p/f, just as the dynamics of intensity change in nature depends fundamentally on the potential intensity (Tang and Emanuel 2012), including for idealized landfall (CC21). Landfall is a transient adjustment between two equilibrium states (CC20), and hence, size will not scale directly with V_p/f or else the storm would shrink to zero size nearly instantaneously, which clearly does not happen even for an instantaneous transition to land (CC21). Thus, we propose the next simplest hypothesis: that size after landfall will scale with v_m/f, where v_m is the maximum wind speed itself. Unlike V_p, which can change instantly, v_m will change over finite time scale and its response may also be predictable theoretically or empirically (CC21). This approach ties storm size to intensity in the transient response in the same manner as it is done at equilibrium via V_p/f. We test this hypothesis below.

For the definition of storm outer size, multiple metrics have been applied to define r_0 in past work, including r_{12} and $r_{\rm 34kt}$, where r_{12} represents the radius of 12 m s^{-1} wind and $r_{\rm 34kt}$ represents the radius of 34 kt (1 kt $\approx$ 0.51 m s^{-1}) azimuthal wind speed. In practice, $r_{\rm 34kt}$ is the outermost wind radius that is commonly estimated in operations (Knapp et al. 2010; NHC 2022) and can be linked directly to r_m via the structural model

Unauthenticated | Downloaded 07/11/23 03:06 AM UTC

TABLE 1. Parameter values of the CM1 CTRL simulation. Only the two boldface parameters C_d and ϵ are modified individually or simultaneously in idealized landfall experiments as described in Fig. 1.

Parameter	Name	Value	Parameter	Name	Value
l_h	Horizontal mixing length	750 m	$T_{\rm ST}$	Surface temperature	300 K
$l_{\rm inf}$	Asymptotic vertical mixing length	100 m	$T_{\rm tpp}$	Tropopause temperature	200 K
C_k	Exchange coefficient of enthalpy	0.0015	$Q_{\rm cool}$	Radiative cooling rate (potential temperature)	1 K day^{-1}
C_d	**Exchange coefficient of momentum**	**0.0015**	*idiss*	Dissipative heating	1 (turned on)
ϵ	**Surface evaporative fraction**	**1**	f	Coriolis parameter	5×10^{-5} s^{-1}
Δx	Horizontal grid spacing	3 km	$H_{\rm domain}$	Height of model top	25 km
Δz	H = 0–3 km: fixed vertical grid spacing	0.1 km	$L_{\rm domain}$	Radius of model outer wall	3000 km
	H = 3–12 km: stretching vertical grid spacing	0.1–0.5 km			
	H = 12–25 km: fixed vertical grid spacing	0.5 km			

described above (Chavas and Knaff 2022). Thus, we choose to focus on $r_{34\rm kt}$ as our outer size metric on practical grounds, as the outer circulation tends to vary coherently (C15).

3. Methodology

a. Idealized landfall simulations

As discussed in CC20 and CC21, spatiotemporal heterogeneity in surface properties are complicated in real-world landfalls, but landfall is fundamentally a transient response to a rapid change in surface wetness and roughness. Here we design simplified landfall experiments in an axisymmetric geometry with a uniform environment and uniform boundary forcing to test the response of a mature TC to modified surface roughness and wetness, individually and in combination. Idealized landfall experiments are performed using the Bryan Cloud Model (CM1v19.8) (Bryan and Fritsch 2002) in an axisymmetric geometry with the same setup as CC21. CM1 solves the fully compressible equations of motion in height coordinates on an f plane on a fully staggered Arakawa C-type grid. Model parameters are summarized in Table 1. This simple approach neglects all water–radiation and temperature–radiation feedbacks (Cronin and Chavas 2019). The simulation results are robust to varying the choice of model resolutions or mixing lengths (CC21). Note that the axisymmetric responses discussed here may be considered akin to a 3D storm in the limit of a very rapid translation speed from uniform ocean to uniform land; asymmetry features will be introduced when heterogeneous surface properties change over a finite time scale beneath the storm (Hlywiak and Nolan 2021, 2022). Detailed explanations and discussions about the model setup can be fully referred to CC21.

We first run a baseline experiment with the above model setup to generate the control experiment (CTRL). The 200-day baseline simulation allows a mature storm to reach a statistical steady state, from which we identify a stable 15-day period and then define the CTRL as the ensemble mean of five 10-day segments of the baseline experiment from this stable period whose start times are each one day apart. Using ensemble data helps to reduce noise and increases the robustness of the results. During this 10-day evolution, a quasi-stable storm is maintained. Then we perform different types of idealized landfall experiments by restarting each of the five CTRL ensemble members with surface wetness and/or roughness modified. Surface wetness is modified by decreasing surface evaporative fraction ϵ, which reduces the surface latent heat fluxes $F_{\rm LH}$ through the decreased surface mixing ratio fluxes F_{qv} in CM1 (sfcphys.F). Surface roughness is modified by increasing the drag coefficient C_d, which alters the surface roughness length z_0 and then the friction velocity u^* for the surface log layer in CM1. Readers are referred to CC20 for full details of the modifications in CM1 experiments. Finally, analogous to the CTRL, the five 10-day segments of each landfall experiment are averaged to reduce noise and yield a single mean response evolution.

The design of the idealized landfall experiments is summarized in Fig. 1. This set of experiments is designed to systematically understand how the TC wind field responds to each surface forcing with varying magnitudes, and how each individual forcing affects the wind field in comparison to applying both forcings simultaneously. Therefore, there are roughening-only experiments (XC_d, warm color boxes), drying-only experiments ($Y\epsilon$, gradient blue boxes), combined experiments ($Y\epsilon XC_d$, gray boxes). Finally, we include a special set of combined experiments ($0V_pXC_d$, gradient green boxes) where both surface sensible and latent heat fluxes are set to zero, which sets V_p to zero, while increasing the roughness. The leading value X indicates the multiplicative enhancement factor applied to surface drag coefficient C_d, while Y is the multiplicative reduction factor applied to the surface evaporative fraction ϵ. The modification in C_d or/and ϵ systematically weakens the CTRL storm, which can be understood via the response of potential intensity, $\tilde{V}_p = V_{p,\rm EXP}/V_{p,\rm CTRL}$ [Eqs. (4)–(6) in CC21; Fig. 1].

The combined experiments are conducted in a way where individual drying and roughening are systematically paired with each other. To compare the role of each forcing under different combined-forcing scenarios, we select two subsets of combined-forcing experiments for deeper analysis: 1) $0.7\epsilon 2C_d$, $0.7\epsilon 10C_d$, $0.1\epsilon 2C_d$, and $0.1\epsilon 10C_d$ (underlined in Fig. 1) represent the extreme combinations where each forcing takes its highest or lowest nonzero magnitude; 2) $0.5\epsilon 2C_d$, $0.25\epsilon 4C_d$, and $0.1\epsilon 8C_d$ represent cases where the individual forcing in a combined experiment have similar contributions to reducing

Unauthenticated | Downloaded 07/11/23 03:06 AM UTC

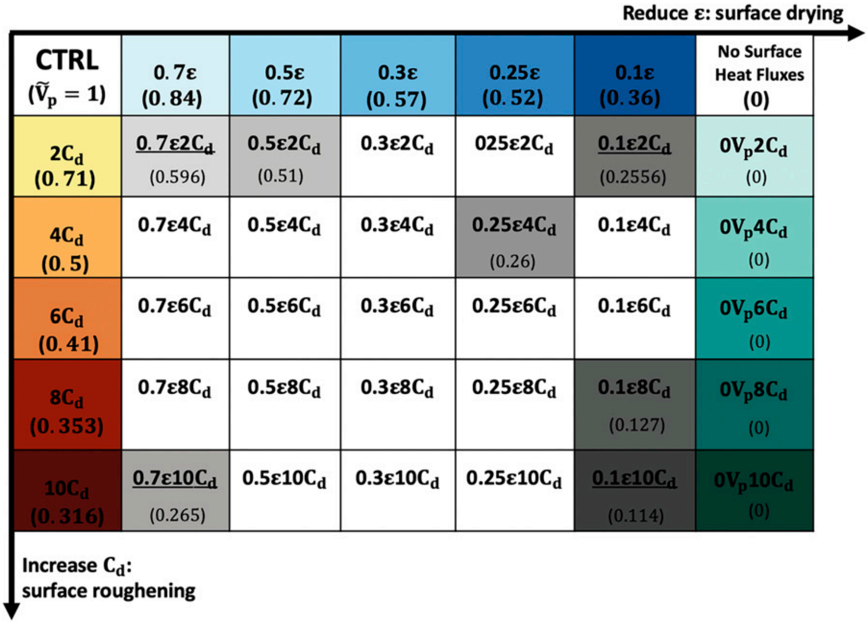

CTRL ($\tilde{V}_p = 1$)	0.7ε (0.84)	0.5ε (0.72)	0.3ε (0.57)	0.25ε (0.52)	0.1ε (0.36)	No Surface Heat Fluxes (0)
$2C_d$ (0.71)	$0.7\varepsilon 2C_d$ (0.596)	$0.5\varepsilon 2C_d$ (0.51)	$0.3\varepsilon 2C_d$	$025\varepsilon 2C_d$	$0.1\varepsilon 2C_d$ (0.2556)	$0V_p2C_d$ (0)
$4C_d$ (0.5)	$0.7\varepsilon 4C_d$	$0.5\varepsilon 4C_d$	$0.3\varepsilon 4C_d$	$0.25\varepsilon 4C_d$ (0.26)	$0.1\varepsilon 4C_d$	$0V_p4C_d$ (0)
$6C_d$ (0.41)	$0.7\varepsilon 6C_d$	$0.5\varepsilon 6C_d$	$0.3\varepsilon 6C_d$	$0.25\varepsilon 6C_d$	$0.1\varepsilon 6C_d$	$0V_p6C_d$ (0)
$8C_d$ (0.353)	$0.7\varepsilon 8C_d$	$0.5\varepsilon 8C_d$	$0.3\varepsilon 8C_d$	$0.25\varepsilon 8C_d$	$0.1\varepsilon 8C_d$ (0.127)	$0V_p8C_d$ (0)
$10C_d$ (0.316)	$0.7\varepsilon 10C_d$ (0.265)	$0.5\varepsilon 10C_d$	$0.3\varepsilon 10C_d$	$0.25\varepsilon 10C_d$	$0.1\varepsilon 10C_d$ (0.114)	$0V_p10C_d$ (0)

FIG. 1. Two-dimensional experimental phase space of surface drying (decreasing ϵ moving left to right) and surface roughening (increasing C_d moving top to bottom). CTRL is an ocean-like surface with $(C_d, \epsilon) = (0.0015, 1)$. Values of the potential intensity response $\tilde{V}_p$ for CTRL, individual drying or roughening, and representative combined experiments are listed in parentheses; $\tilde{V}_p$ for any combination of forcing is the product of $\tilde{V}_p$ for each individual forcing. Representative experiments testing combined forcings are shaded gray and the subset testing the most extreme combinations of each forcing are underlined. Experiment set $0V_pXC_d$, corresponding to the special case where surface heat fluxes are entirely removed ($V_p = 0$), are shaded green.

V_p. Finally, the experiment set $0V_pXC_d$ demonstrates how the magnitude of C_d changes the wind field decay when V_p is uniformly reduced to zero across the experiments. This simplified setup could be more useful for practical application to the real-world landfalls since no final equilibrium V_p estimation is required (CC21).

b. *Testing theory against simulations*

The near-surface wind field drives inland TC hazards. Thus, the evolution of the 10-m wind field in different types of idealized landfall experiments is compared to the C15 model prediction. The transient response of the TC wind field in each idealized landfall experiment and the corresponding physical mechanisms were analyzed in CC20. CC20 found that in response to surface roughening, storm size (r_m and $r_{34\mathrm{kt}}$) decrease rapidly along with v_m as the entire wind field weakened and shrank. In contrast, in response to surface drying, v_m decreased rapidly while size, including the broad outer circulation, remained relatively constant, due to the relatively slow response to the stabilization of the overturning circulation.

We focus principally on the first 24 h of the evolution, during which the wind field response to each landfall type is the strongest while the circulation remains sufficiently well defined to easily identify $r_{34\mathrm{kt}}$ (Fig. 2). A stable gale wind radius is often no longer observable 24 h after TC landfall in the real world (Jing and Lin 2019). We compare model versus simulation at $\tau = 1$, 6, 12, and 24 h where τ denotes the time since the start of a given forcing experiment, and we display results whenever a value of $r_{34\mathrm{kt}}$ is still discernible. Though the C15 model is not a forecast model, here we aim to test to what extent the C15 model can reproduce the simulated wind field response given the time-dependent responses of intensity, size, and the change in C_d in our experiments. For the C15 prediction, the simulated $v_m(\tau)$ and $r_{34\mathrm{kt}}(\tau)$ response of each experiment are used to fit the structural model. We hold C_k fixed at its CTRL value ($C_k = 0.0015$) and set C_d to be its modified value for each experiment. Since latitude typically varies minimally for a landfalling TC over a 24-h period, the Coriolis parameter f is held fixed at its CTRL value (5×10^{-5} s^{-1}). The radiative-subsidence rate W_{cool} is set to 0.002 m s^{-1}, which is the median of the best-fit value for observed storms (C15). The wind field solution is not very sensitive to W_{cool} except for at large radii well beyond $r_{34\mathrm{kt}}$ (online supplementary Fig. 1). For TC size, we test the simple hypothesis

$$r_{34\mathrm{kt}}(\tau) \sim \frac{v_m(\tau)}{f} \tag{6}$$

that was motivated in the previous section. Since we hold f constant, this hypothesis simplifies to

$$\tilde{r}_{34\mathrm{kt}}(\tau) \sim \tilde{v}_m(\tau). \tag{7}$$

Unauthenticated | Downloaded 07/11/23 03:06 AM UTC

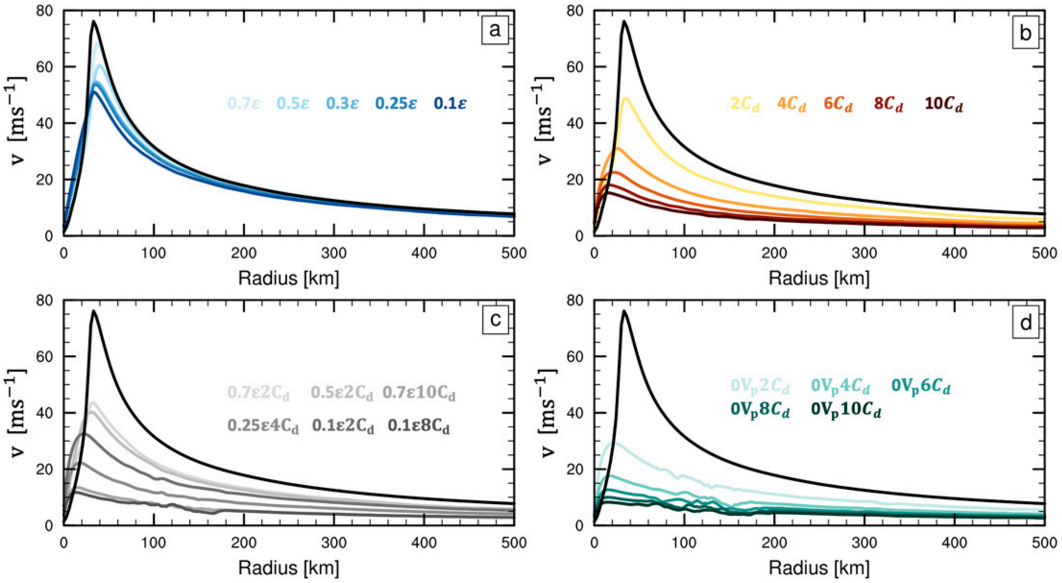

FIG. 2. The simulated 10-m wind field in response to different magnitudes of each type of idealized landfall (colored lines) at $\tau = 24$ h. The initial CTRL wind field is shown by the thick black line in each plot.

As in CC21, we analyze results as responses relative to initial state. Hence, the intensity and size in each experiment are normalized by the CTRL value, i.e., $\tilde{v}_m = v_{m,\mathrm{EXP}}/v_{m,\mathrm{CTRL}}$ and $\tilde{r}_{34\mathrm{kt}} = r_{34\mathrm{kt,EXP}}/r_{34\mathrm{kt,CTRL}}$. That is, we examine whether the simulated transient response of intensity can predict the transient response of storm outer size during the decay evolution.

4. Results

a. TC structure

We first examine to what extent the C15 model can reproduce the response of the storm wind field structure in our idealized landfall experiments, with intensity and size taken as their simulated values. Figure 3 shows the C15 model and its inner and outer component models against our CM1 CTRL simulation. The model inputs are the CM1 CTRL values of v_m and $r_{34\mathrm{kt}}$. We set f to 0.000 05 s^{-1}, $W_{\mathrm{cool}} = 0.002$ m s^{-1}, and C_d is 0.0015. In this example, the model does very well predicting the simulated wind profile for nearly the entire circulation beyond r_m, but it underestimates r_m, which will be discussed below.

Figure 4 compares the C15 prediction fit to (v_m, $r_{34\mathrm{kt}}$) against the model simulation for representative idealized landfall experiments 0.25ϵ, 4C_d, 0.25ϵ4C_d, and 0V_p4C_d at $\tau = 1$, 6, 12, and 24 h. The wind field difference between C15 prediction and model simulation across all the experiments are shown in Fig. 5.

For surface drying only (Fig. 4a), C15 does well in reproducing much of the wind field beyond 2r_m out to large radii ($r = 800$ km) during the slow decay. The model generally underestimates the wind speed within the convective inner region ($r \leq 200$ km) due to the low bias in r_m that persists and acts to shift the peak wind region slightly inward of the simulation. At $\tau = 24$ h, the low bias near r_m becomes much smaller for stronger drying (0.3ϵ, 0.25ϵ, 0.1ϵ in Figs. 4a and 5a). Beyond $r_{34\mathrm{kt}}$, the C15 prediction bias is less than 2 m s^{-1} across all the drying experiments (Fig. 4a). For experiments that include surface roughening (i.e., roughening only, combined, and 0V_pXC_d), the C15 prediction performs well in reproducing the wind field evolution at all radii beyond r_m (Figs. 4b–d). The negative r_m bias at the initial time step decreases over the first 12 h and becomes a slightly positive r_m bias through 24 h (Figs. 4b–d and 5b–d). The wind field bias is generally less than 2 m s^{-1} outside $r_{34\mathrm{kt}}$ across all the roughening and combined

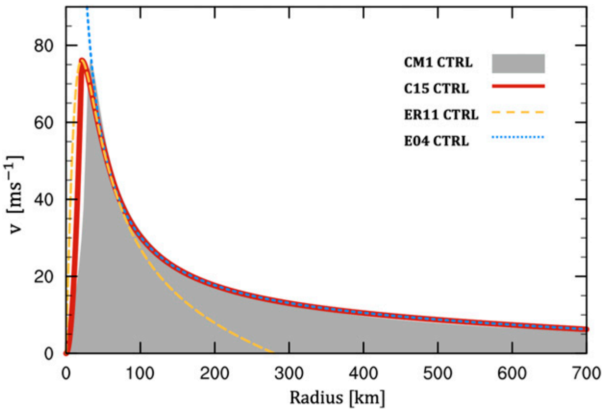

FIG. 3. The 10-m wind field of the CM1 simulated steady-state, mature storm (shaded CM1 CTRL), the ER11-predicted wind profile (yellow dashed), the E04-predicted wind profile (blue dashed), and the C15-predicted wind profile (red solid). $f = 5 \times 10^{-5}$ s^{-1}, $\chi = 1.5$, where $C_d = 0.0015$ and $W_{\mathrm{cool}} = 0.002$ m s^{-1}. $v_m = 76.1$ m s^{-1}, $r_m = 33$ km, and $r_{34\mathrm{kt}} = 202$ km in the CM1 CTRL simulation.

Unauthenticated | Downloaded 07/11/23 03:06 AM UTC

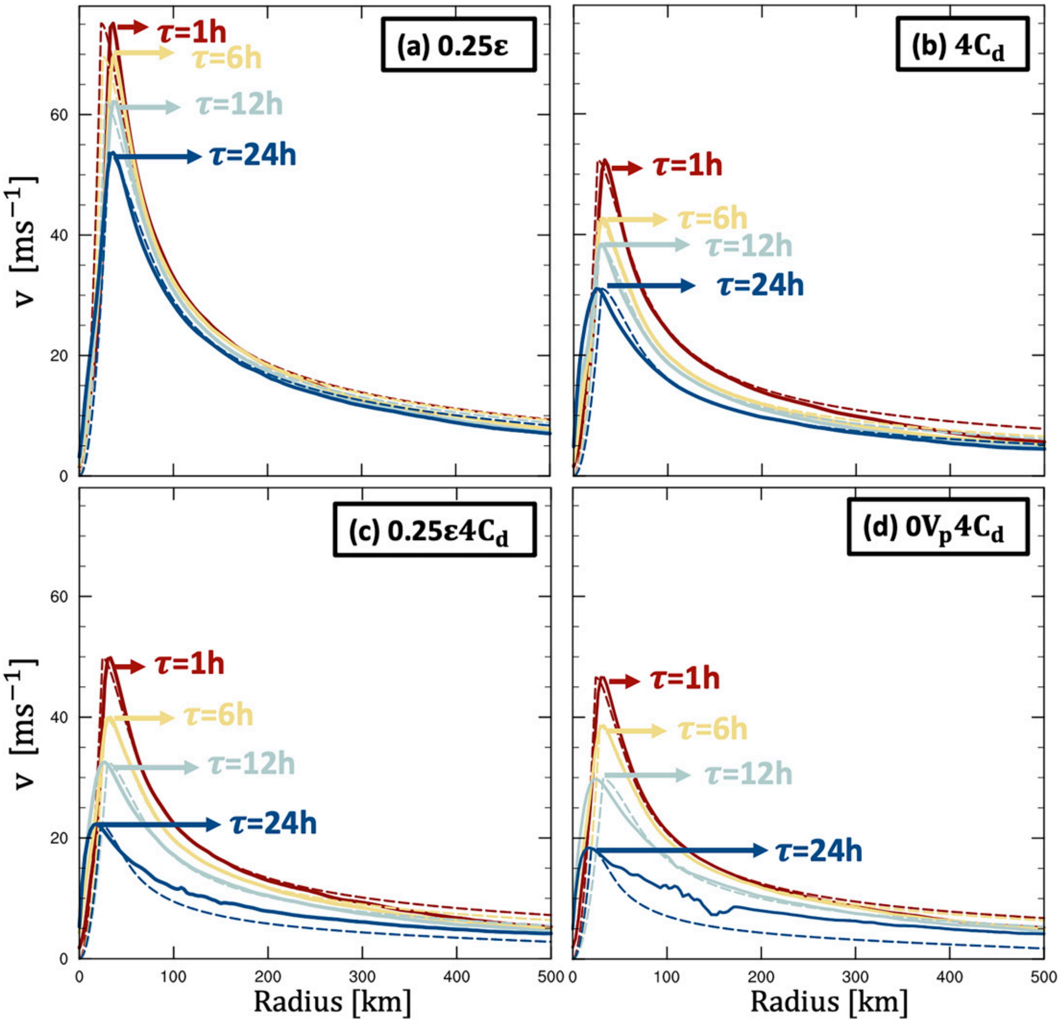

FIG. 4. The 10-m wind field of the representative landfall experiments (a) 0.25ϵ, (b) 4C_d, (c) 0.25ϵ4C_d, and (d) $0V_p4C_d$ at τ = 1, 6, 12, and 24 h. Colored curves are the simulated wind field (solid) and C15-predicted wind field (dashed).

experiments (Figs. 5b,c) similar to drying-only experiments. In $0V_pXC_d$ experiments, the C15 prediction underestimates the outer wind field when v_m is decreased toward 34 kt at $\tau = 24$ h (Figs. 4d and 5d) with a bias larger than 2 m s^{-1}. For $r < r_m$, the wind profile gradually transitions from concave to convex, and as a result C15 underestimates the winds after 12 h. Though for hazard footprints, the wind profile within the eyewall is not critical since these locations must also experience the stronger winds from the eyewall immediately before and after. A model for the wind profile inside r_m during the landfall could be developed to better depict the entire wind field.

Overall, this simple theory-based model reproduces the wind field response to idealized landfalls given a small number of physical, observable input parameters. The outer circulation in drying-only experiments is well captured throughout the evolution. With moderate or stronger surface roughening, which is more like the real world, the C15 model well reproduces the simulated wind field beyond r_m before the storm dissipates and loses its structure.

In experiments with surface roughening, the mismatched wind profile within the eye during the later period might arise from the limitations of the C15 model itself: when the storm remains strong during the initial period, the concave inner wind profile within the eye is well described by a quadratic profile. During later stages, the storm is largely weakened by surface roughening, and its inner wind profile transforms from a concave shape to a convex shape more rapidly than in the drying-only experiments, as found in Hlywiak and Nolan (2021) as well. This behavior cannot be captured by a quadratic profile.

b. *TC size*

We next examine to what extent the transient response of size $\tilde{r}_{34\mathrm{kt}}(\tau)$ scales with the transient response of intensity $\tilde{v}_m(\tau)$ in individual-forcing experiments (Fig. 6a), combined-forcing experiments (Fig. 6b), and $0V_pXC_d$ experiments (Fig. 6c) throughout the 48-h evolution. For cases with strong surface

Unauthenticated | Downloaded 07/11/23 03:06 AM UTC

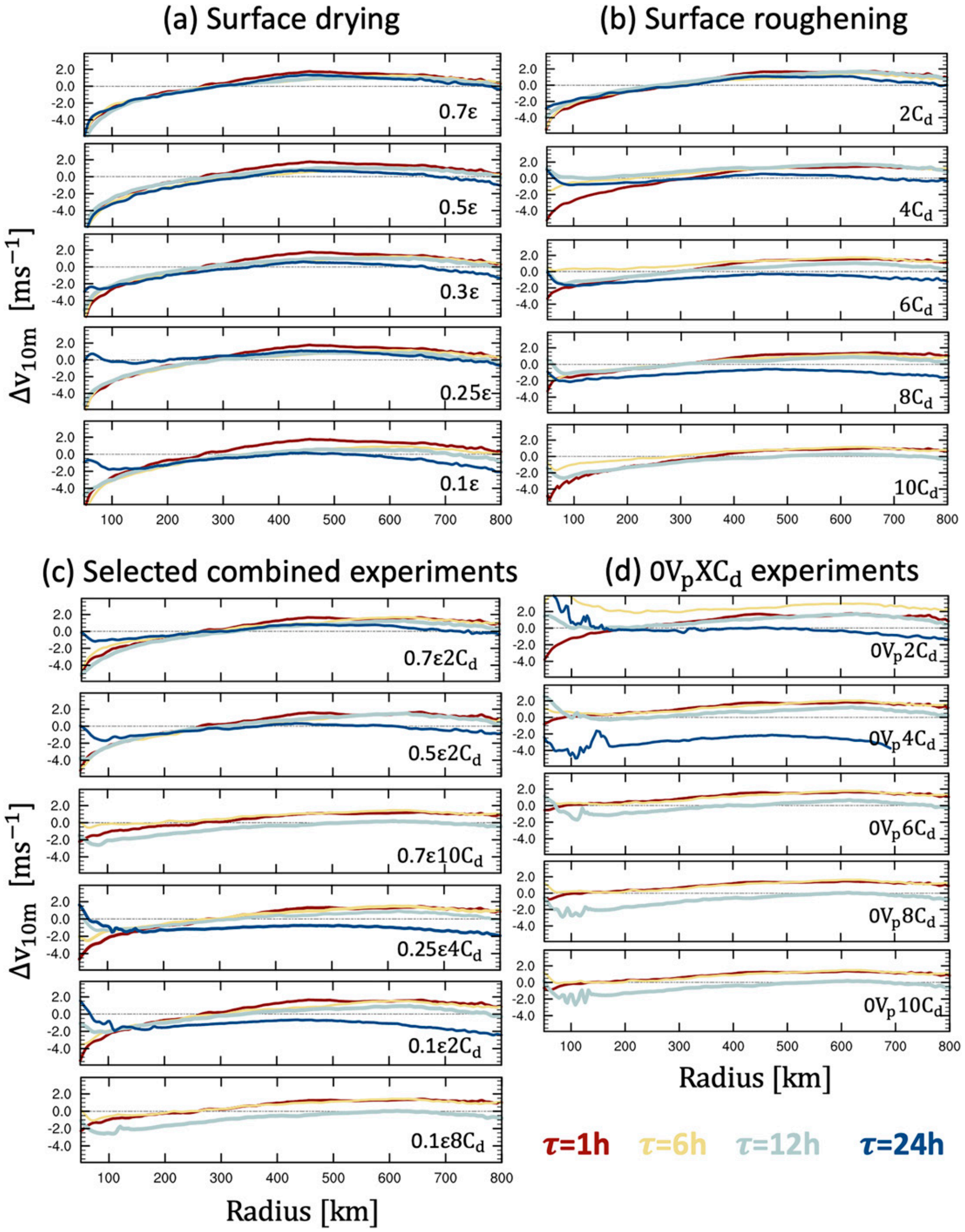

FIG. 5. The wind field difference between C15 prediction and the idealized landfall simulation from $r = 50$ to 800 km across all the experiments of (a) surface drying experiments, (b) surface roughening experiments, (c) combined experiments, and (d) $0V_pXC_d$ experiments at $\tau = 1$, 6, 12, and 24 h. Each τ is indicated by the same color as in Fig. 4.

roughening ($8C_d$, $10C_d$, $0.7\epsilon10C_d$, $0.1\epsilon8C_d$, $0.1\epsilon10C_d$, and $0V_p8C_d$, $0V_p10C_d$), simulated intensity quickly decreases below 34 kt after $\tau = 12$ h, and thus, their corresponding long-term $\tilde{r}_{34\mathrm{kt}}(\tau) \sim \tilde{v}_m(\tau)$ relationship is not shown in Fig. 6.

For roughening experiments (Fig. 6a, warm colors), $\tilde{r}_{34\mathrm{kt}}$ scales very closely with $\tilde{v}_m$ throughout the 48 h period, and it does so consistently across all experiments. For $\tau = 24$–48 h, $\tilde{v}_m$ gradually equilibrates while $\tilde{r}_{34\mathrm{kt}}$ continues to decrease slowly. Thus, there is a slight deviation away from the scaling toward the end of the evolution.

For drying experiments (Fig. 6a, blue colors), $\tilde{r}_{34\mathrm{kt}}$ scales reasonably closely with $\tilde{v}_m$ by the end of the 48 h period.

Unauthenticated | Downloaded 07/11/23 03:06 AM UTC

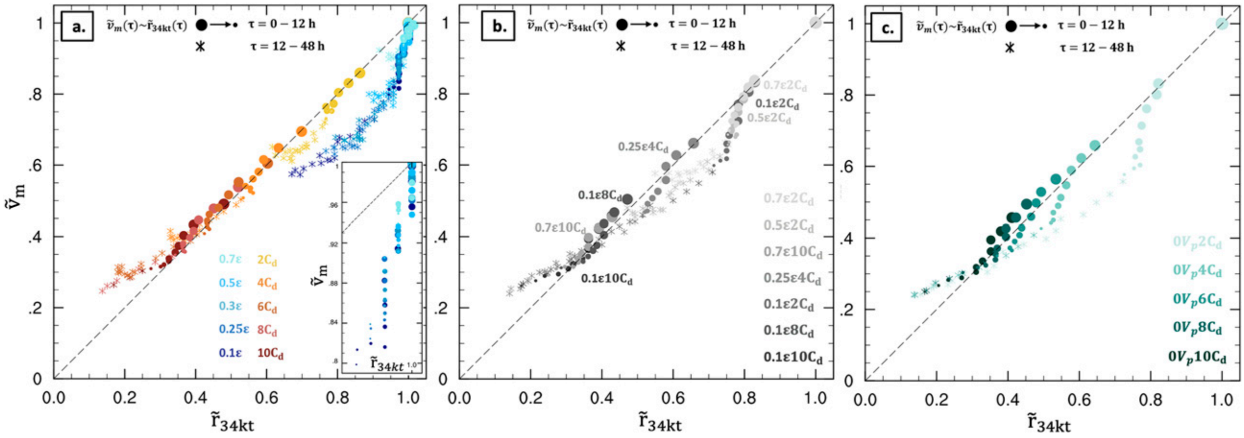

FIG. 6. The relationship between $\tilde{v}_m(\tau)$ and $\tilde{r}_{34\mathrm{kt}}(\tau)$ during a 48-h evolution (asterisks mark every 2 h) for (a) individual forcing experiments, (b) combined experiments, and (c) $0V_pXC_d$ experiments. The subplot in (a) emphasizes on the relationship between $\tilde{v}_m(\tau)$ and $\tilde{r}_{34\mathrm{kt}}(\tau)$ during the first 12-h period for all surface drying experiments. For $0V_pXC_d$ experiments with stronger surface roughening ($0V_p8C_d$, $0V_p10C_d$), the relationship no longer exits after τ = 24 h due to the rapid decay.

However, during the first 12 h, the storm intensity principally weakens while its outer size shrinks very slowly (Fig. 6a, subplot) as found in CC20. After that, size shrinks steadily with the decreasing intensity, scaling closely with one another from τ = 12–36 h. During the final 12 h, size continues to gradually shrink as the intensity begins to equilibrate. Thus, $\tilde{r}_{34\mathrm{kt}}$ scales more closely with $\tilde{v}_m$ by τ = 48 h, at which time $\tilde{r}_{34\mathrm{kt}}$ is approximately 10%–15% larger than $\tilde{v}_m$ across all the drying experiments. The trajectories through ($\tilde{v}_m$, $\tilde{r}_{34\mathrm{kt}}$) space is consistent across all experiments similar to the roughening experiments.

For the combined experiments (Fig. 6b) and the $0V_pXC_d$ experiments (Fig. 6c), the storm size response $\tilde{r}_{34\mathrm{kt}}(\tau)$ also generally scales with the intensity response $\tilde{v}_m(\tau)$ throughout the evolution, especially with at least moderate roughening. For experiments with relatively weaker roughening than drying ($0.5\epsilon2C_d$, and $0.1\epsilon2C_d$ in Fig. 6b, $0V_p2C_d$ and $0V_p4C_d$ in Fig. 6c), $\tilde{v}_m(\tau)$ and $\tilde{r}_{34\mathrm{kt}}(\tau)$ are less linearly related while exhibiting both characteristics of surface drying (initially faster weakening than shrinking) and roughening experiments (weakening and shrinking scale together). Specifically, during the initial period (τ = 0–6 h), $\tilde{r}_{34\mathrm{kt}}(\tau)$ decreases sharply and nearly linearly with $\tilde{v}_m(\tau)$ across all the experiments, as seen in pure roughening. For τ = 6–12 h, the storm weakens while size remains relatively steady. After τ = 12 h, size steadily decreases again as the storm weakens, as seen in pure drying. For τ out to 48 h, the trajectories return toward a close scaling between intensity and size responses similar to roughening, particularly in the presence of at least moderate roughening.

Next, we test the extent to which the response of storm size for combined forcing can be predicted from the responses to surface roughening and drying individually. As found in CC21, the complete time-dependent response of storm intensity to simultaneous surface roughening and drying, $\tilde{v}_{m,C_d\epsilon}(\tau)$, can be predicted by the product of the individual response, $v^*(\tau)$, as

$$\tilde{v}_{m,C_d\epsilon}(\tau) \approx \tilde{v}^*(\tau) = \tilde{v}_{m,C_d}(\tau)\tilde{v}_{m,\epsilon}(\tau). \tag{8}$$

Given that we find that $\tilde{r}_{34\mathrm{kt}}(\tau)$ scales reasonably well with $\tilde{v}_m(\tau)$, we propose a similar hypothesis here for the size response in combined experiments as

$$\tilde{r}_{34\mathrm{kt},C_d\epsilon}(\tau) \approx \tilde{r}^*(\tau) = \tilde{r}_{34\mathrm{kt},C_d}(\tau)\tilde{r}_{34\mathrm{kt},\epsilon}(\tau), \tag{9}$$

and assume that

$$\tilde{v}^*(\tau) \sim \tilde{r}^*(\tau). \tag{10}$$

The hypotheses proposed in Eqs. (9) and (10) are tested against our representative combined simulations (Fig. 7). First we compare the predicted responses $\tilde{r}^*(\tau)$ and $\tilde{v}^*(\tau)$ to the corresponding simulated responses, $\tilde{r}_{34\mathrm{kt}}(\tau)$ and $\tilde{v}_m(\tau)$, of the combined experiments (Fig. 7, red pentagrams and dots) at τ = 0, 6, 12, 24, 36, and 48 h. Overall, the predicted size–intensity relationship $\tilde{r}^*(\tau) \sim \tilde{v}^*(\tau)$ closely follows the simulated relationship $\tilde{r}_{34\mathrm{kt}}(\tau) \sim \tilde{v}_m(\tau)$ throughout the evolution across all the combined experiments. The relationship is again strongest in the presence of at least moderate roughening. In experiments with stronger surface drying and weaker surface roughening (Figs. 7c,e–g), the prediction (red pentagrams) deviates from the simulation (red dots) from τ = 12 to 36 h, with $\tilde{v}^*(\tau)$ decreasing to smaller values than the simulated $\tilde{v}_m(\tau)$.

Finally, we identify the dominant forcing for driving the responses in $\tilde{v}_m(\tau)$ and $\tilde{r}_{34\mathrm{kt}}(\tau)$ in our combined experiments by comparing the combined experiments to individual-forcing experiments. Overall, the outer size responses in the combined experiment and the analogous roughening-only experiment with identical C_d are similar from τ = 0 to 12 h, during which size and intensity change most strongly, before deviating thereafter (Fig. 7, red and gray dots). This consistency suggests that the size response is primarily dominated by surface roughening, regardless of its magnitude or the concurrent magnitude of drying. This is consistent with the findings of CC20 that size does not feel the effects of surface drying in the first 12 h, whereas size responds immediately to surface

Unauthenticated | Downloaded 07/11/23 03:06 AM UTC

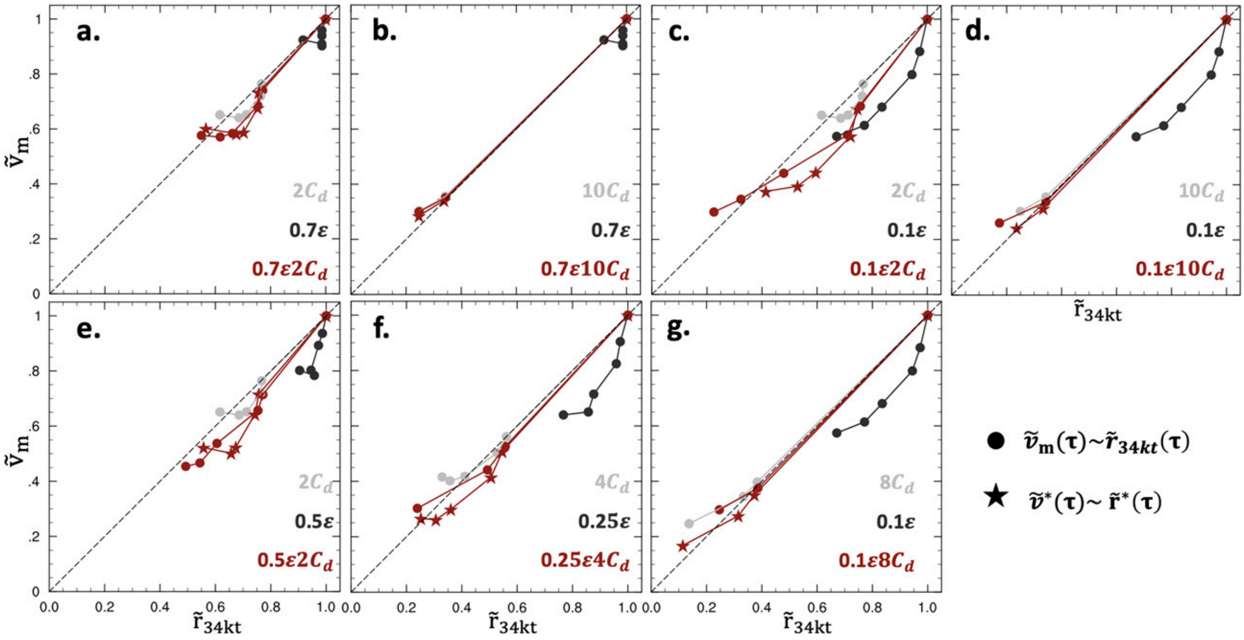

FIG. 7. The relationship between simulated $\tilde{v}_m(\tau)$ and $\tilde{r}_{34\text{kt}}(\tau)$ for different combined experiments and their corresponding deconstructed individual forcing experiments at $\tau = 0$, 6, 12, 24, 36, and 48 h, as long as $\tilde{r}_{34\text{kt}}(\tau)$ still exist in the experiment. The predicted $\tilde{v}^*(\tau)$ and $\tilde{r}^*(\tau)$ relationship [Eqs. (8)–(10)] of each combined experiment are marked by pentagrams at the same τ as the simulated results. Here (a) 0.7ϵ2C_d, (b) 0.7ϵ10C_d, (c) 0.1ϵ2C_d, and (d) 0.1ϵ10C_d are representative combined experiments where each individual forcing takes its highest or lowest nonzero magnitude. (e) 0.5ϵ2C_d, (f) 0.25ϵ4C_d, and (g) 0.1ϵ8C_d are representative combined experiments where the magnitude of individual forcing in a combined experiment yields similar contribution to the intensity response.

roughening. However, for experiments with relatively weaker surface roughening (0.7ϵ2C_d, 0.5ϵ2C_d, 0.1ϵ2C_d, and 0.25ϵ4C_d as shown in Figs. 7a,c,e,f), surface drying imposes an impact on the intensity–size relationship primarily during an early stage ($\tau = 6$–12 h) and final stage ($\tau > 36$ h). In early stage, $\tilde{v}_m(\tau)$ decreases more than the $\tilde{r}_{34\text{kt}}(\tau)$ in these combined experiments compared to the roughening-only experiments. In the final stage after the storm has already weakened considerably, $\tilde{v}_m(\tau)$ and $\tilde{r}_{34\text{kt}}(\tau)$ in combined experiments decreases more than the corresponding roughening-only experiments before reaching the equilibrium.

To summarize, $r_{34\text{kt}}(\tau)$ scales quite closely with $v_m(\tau)$ for mature storms in response to idealized landfall, especially for a rougher land surface. For drying-only and weaker-roughening cases, the theory fits a bit less well due to slower shrinking than weakening during the first 24 h before shrinking accelerates. These findings provide some evidence for our hypothesis that the equilibrium size length scale on the f plane becomes important for the dynamics of the transition to land. Testing the role of β lies beyond the scope of this work. The above results suggest that a viable simple prediction of the storm outer size for any combination of surface drying and roughening magnitudes can be made if given an estimate of the intensity response [Eq. (10)]. In the real world, C_d of the land surface is typically much more than 4 times higher than the ocean surface [C_d is calculated from Eq. (13) in Hersbach (2010) using the ERA5 surface roughness length data]. Thus, with such strong roughening, the theoretical $r_{34\text{kt}}(\tau)$ prediction may be directly applicable to real-world landfalls too.

All our results taken together suggest the potential to predict the complete wind field evolution to idealized landfall if given the intensity response. We explore this avenue next.

c. A model for the wind field in idealized landfalls

Finally, we combine the findings for modeling structure and size in this work to predict the responses of the near-surface wind field and compare them against our subsets of combined-forcing landfall experiments.

We model the wind field using the C15 model with inputs as described above, which requires the temporal evolution of intensity and size. To first focus on evaluating our predictions for size and structure, here we take the simulated intensity evolution $v_m(\tau)$ to serve as a "perfect" intensity model. We predict the outer size response $\tilde{r}_{34\text{kt}}(\tau)$ by assuming it scales directly with $\tilde{v}_m(\tau)$ as in Eq. (7). Theory is compared to the simulation for each experiment at $\tau = 6$ h (Figs. 8a,c) and 24 h (Figs. 8b,d). For the latter, experiments 0.1ϵ8C_d, 0.7ϵ10C_d, 0V_p6C_d, 0V_p8C_d, and 0V_p10C_d are excluded at $\tau = 24$ h since their corresponding intensity quickly decreases below 34 kt (Figs. 8b,d).

Overall, the wind field model prediction performs reasonably well in capturing the simulated wind field response across all experiments. The prediction of r_m itself is imperfect, especially for experiments with weak surface roughening (Fig. 8), since the model begins with the low bias in r_m from CTRL. For weak roughening (Figs. 8b,d), as v_m decreases toward 34 kt,

Unauthenticated | Downloaded 07/11/23 03:06 AM UTC

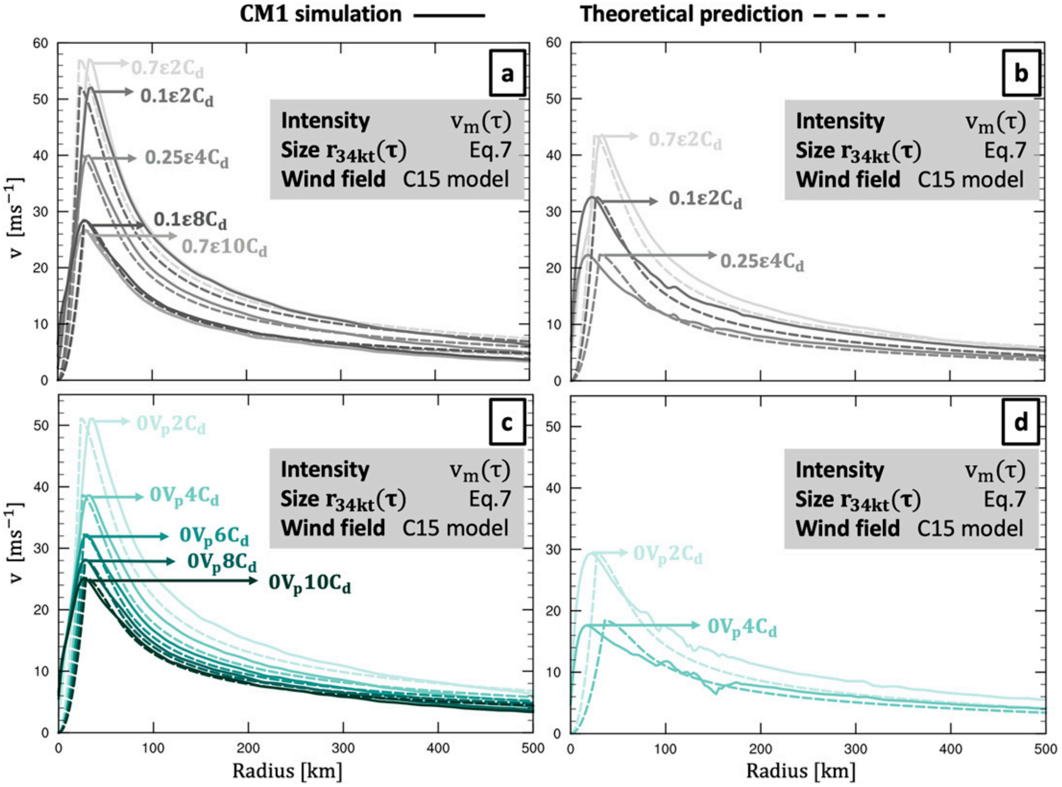

FIG. 8. Comparison of the simulated wind field of combined-forcing landfall experiments (solid) and the corresponding theoretical prediction (dashed) at (a),(c) $\tau = 6$ h and (b),(d) $\tau = 24$ h. The theoretical prediction applies the simulated intensity response $v_m(\tau)$ and the corresponding size prediction $r_{34kt}(\tau)$ [Eq. (7)] in the C15 model. Experiments with stronger surface modifications decay too fast to produce the input v_m and r_{34kt} for C15 model at $\tau = 24$ h; thus, those experiments ($0.1\epsilon8C_d$, $0.7\epsilon10C_d$ and $0V_p6C_d$, $0V_p8C_d$, $0V_p10C_d$) are not shown in (b) and (d).

the model more strongly underestimates the simulated r_m. For strong roughening, though, (Figs. 8a,c) this inner-core bias tends to decrease with time.

Here we have used the simulated intensity evolution directly, but this evolution could also be predicted via a statistical model such as Jing and Lin (2019), a numerical weather prediction model forecast, or a theory-based model such as that proposed in CC21. We also tested this simple wind field model using the intensity model of CC21 $v^*_{th}(\tau)$ introduced in CC21 [Eqs. (14) and (15) therein] and its corresponding size estimation r^*_{th} via Eq. (10) (supplementary Fig. 2). This approach also works reasonably well, though it still requires specification of the boundary layer depth parameter, which is poorly constrained as described in CC21. Hence, we have focused here on taking the intensity evolution as known in order to focus on evaluating our predictions for size and structure. In practice, an intensity model would be required to make a true prediction.

To summarize, given the TC intensity and r_{34kt} prior to landfall and knowledge of the idealized land surface conditions, one can predict the first-order postlandfall wind field evolution. Notably, in contrast to the intensity decay model of CC21, which depends on a poorly understood boundary layer height parameter, the size and structure results presented here do not depend on any free parameters and hence are expected to apply generally. This simple model may serve as a foundation for a model to predict the wind field response to landfall that further incorporates the many additional complexities associated with real-world landfalls.

5. Summary and discussion

This work proposes a simple theory-based model for the response of the tropical cyclone wind field to idealized landfalls and tests it against numerical simulation experiments. The model combines an existing physics-based model for the wind field and a simple model for storm outer size $r_{34kt}(\tau)$ that assumes it follows the response of maximum wind speed $v_m(\tau)$. Combining these results with a prediction for TC intensity yields a theoretical model for inland TC wind field. Key findings are as follows:

- Given simulated v_m and r_{34kt}, the C15 wind field model [Eqs. (1)–(5)] generally reproduces the response of the wind field beyond r_m to idealized landfalls over the first 24 h, which is the period of most significant weakening. For the convecting inner-core region near r_m, the C15 model is not able to precisely predict the r_m, though this is due in part to a bias in the initial profile itself. For the convection-free outer region, the C15 prediction generally reproduces the

Unauthenticated | Downloaded 07/11/23 03:06 AM UTC

wind field response to various forcings with minimal bias over much of the circulation beyond $r = 50$ km.
- The landfall response of storm size $r_{34\mathrm{kt}}(\tau)$ is found to scale closely with that of storm intensity $v_m(\tau)$ [Eq. (7)], particularly in the presence of relatively strong roughening. This finding aligns with the hypothesis that the equilibrium storm size length scale, V_p/f, becomes important in the dynamics of the transition to land where V_p becomes near zero.
- The storm size response to combined drying and roughening can be deconstructed as the product of the responses to each individual forcing [Eqs. (8)–(10)], similar to intensity as found in CC21. Surface roughening imposes a strong and rapid initial response and hence dominates the size response within the first 12 h regardless of the magnitude of drying, while the longer-term size change is gradually affected by surface drying too.
- Given the intensity evolution, the transient response of the wind field to idealized landfalls can be predicted reasonably well by combining simple models for storm structure [Eqs. (1)–(5)] and the responses of outer size [Eq. (7)].
- These results for size and structure may be quite general, as they do not depend on any free parameters. This is in contrast to the intensity model presented in CC21 that depends on an uncertain boundary layer depth. Considering that inland surface roughness is much higher than ocean surface in the real world, the above findings may be applicable to real-world landfalls.

These findings suggest that a simple theory-based model may be useful for a first-order prediction of the tropical cyclone wind field after landfall. It offers an efficient approach to generate the complete TC wind profile with limited known environmental parameters. Though systematic bias is difficult to avoid, one can use empirical adjustment to reduce or eliminate the system bias depending on the application purpose (Chavas and Knaff 2022). Landfall in the real world is complicated, though. This series of studies (CC20, CC21, and the present work) removes the additional complexities existed in the real landfalls to focus on the most fundamental processes associated with landfall. The model serves as a baseline for future testing how key additional complexities, such as finite translation speed (Hlywiak and Nolan 2021, 2022), surface heterogeneity, and asymmetries, modify the wind field response after landfall.

For real-world storms, the C15 model has been found to perform best among existing wind field models in retrospective simulations of observed storm tide (S. Wang et al. 2022). It is a natural next step to examine the validity of this theory-based model against the complicated real-world postlandfall storms. Our preliminary comparisons against the inland wind field from reanalysis data show promising results. Future work seeks to more comprehensively examine the model against postlandfall observations and simulations, since a first-order wind field prediction of real-world storms after landfall is essential for improving the modeling of inland hazards both operationally and in long-term risk assessment.

Acknowledgments. The authors were supported by National Science Foundation Grants 1945113 and 1826161. The authors benefited from conversations and advice from Drs. Kerry Emanuel, Frank D. Marks, Daniel T. Dawson, and Richard H. Grant. We also appreciate the feedback and conversations related to this research during the 35th AMS Conference on Hurricanes and Tropical Meteorology and the Symposium on Hurricane Risk in a Changing Climate 2022. Computing resources for this work were generously supported by Purdue's Rosen Center for Advanced Computing and the Community Cluster Program (McCartney et al. 2014). Finally, we thank anonymous reviewers for their constructive feedback that improved this manuscript.

Data availability statement. Datasets of relevant simulated variables from this work are archived on Purdue University Research Repository (PURR) at https://purr.purdue.edu/publications/4199/1, doi:10.4231/3AKW-VX52. We also provide the information needed to replicate the simulations. The code for the C15 wind structure model is available at https://doi.org/doi:10.4231/CZ4P-D448.

REFERENCES

Anthes, R. A., 1974: The dynamics and energetics of mature tropical cyclones. *Rev. Geophys.*, **3**, 495–522, https://doi.org/10.1029/RG012i003p00495.

Bryan, G. H., and J. M. Fritsch, 2002: A benchmark simulation for moist nonhydrostatic numerical models. *Mon. Wea. Rev.*, **130**, 2917–2928, https://doi.org/10.1175/1520-0493(2002)130<2917:ABSFMN>2.0.CO;2.

Chavas, D. R., and K. A. Emanuel, 2010: A QuikSCAT climatology of tropical cyclone size. *Geophys. Res. Lett.*, **37**, L18816, https://doi.org/10.1029/2010GL044558.

——, and ——, 2014: Equilibrium tropical cyclone size in an idealized state of axisymmetric radiative–convective equilibrium. *J. Atmos. Sci.*, **71**, 1663–1680, https://doi.org/10.1175/JAS-D-13-0155.1.

——, and N. Lin, 2016: A model for the complete radial structure of the tropical cyclone wind field. Part II: Wind field variability. *J. Atmos. Sci.*, **73**, 3093–3113, https://doi.org/10.1175/JAS-D-15-0185.1.

——, and K. A. Reed, 2019: Dynamical aquaplanet experiments with uniform thermal forcing: System dynamics and implications for tropical cyclone genesis and size. *J. Atmos. Sci.*, **76**, 2257–2274, https://doi.org/10.1175/JAS-D-19-0001.1.

——, and J. A. Knaff, 2022: A simple model for predicting the tropical cyclone radius of maximum wind from outer size. *Wea. Forecasting*, **37**, 563–579, https://doi.org/10.1175/WAF-D-21-0103.1.

——, N. Lin, and K. A. Emanuel, 2015: A model for the complete radial structure of the tropical cyclone wind field. Part I: Comparison with observed structure. *J. Atmos. Sci.*, **72**, 3647–3662, https://doi.org/10.1175/JAS-D-15-0014.1.

——, ——, W. Dong, and Y. Lin, 2016: Observed tropical cyclone size revisited. *J. Climate*, **29**, 2923–2939, https://doi.org/10.1175/JCLI-D-15-0731.1.

Chen, J., and D. R. Chavas, 2020: The transient responses of an axisymmetric tropical cyclone to instantaneous surface roughening and drying. *J. Atmos. Sci.*, **77**, 2807–2834, https://doi.org/10.1175/JAS-D-19-0320.1.

Unauthenticated | Downloaded 07/11/23 03:06 AM UTC

——, and ——, 2021: Can existing theory predict the response of tropical cyclone intensity to idealized landfall? *J. Atmos. Sci.*, **78**, 3281–3296, https://doi.org/10.1175/JAS-D-21-0037.1.

Cronin, T. W., and D. R. Chavas, 2019: Dry and semidry tropical cyclones. *J. Atmos. Sci.*, **76**, 2193–2212, https://doi.org/10.1175/JAS-D-18-0357.1.

Emanuel, K. A., 2004: Tropical cyclone energetics and structure. *Atmospheric Turbulence and Mesoscale Meteorology*, E. Fedorovich, R. Rotunno, and B. Stevens, Eds., Cambridge University Press, 165–192.

——, 2012: Self-stratification of tropical cyclone outflow. Part II: Implications for storm intensification. *J. Atmos. Sci.*, **69**, 988–996, https://doi.org/10.1175/JAS-D-11-0177.1.

——, 2022: Tropical cyclone seeds, transition probabilities, and genesis. *J. Climate*, **35**, 3557–3566, https://doi.org/10.1175/JCLI-D-21-0922.1.

——, and R. Rotunno, 2011: Self-stratification of tropical cyclone outflow. Part I: Implications for storm structure. *J. Atmos. Sci.*, **68**, 2236–2249, https://doi.org/10.1175/JAS-D-10-05024.1.

Frank, W. M., 1977: The structure and energetics of the tropical cyclone: II. Dynamics and energetics. *Mon. Wea. Rev.*, **105**, 1136–1150, https://doi.org/10.1175/1520-0493(1977)105<1136:TSAEOT>2.0.CO;2.

Frisius, T., D. Schonemann, and J. Vigh, 2013: The impact of gradient wind imbalance on potential intensity of tropical cyclones in an unbalanced slab boundary layer model. *J. Atmos. Sci.*, **70**, 1874–1890, https://doi.org/10.1175/JAS-D-12-0160.1.

Hersbach, H., 2010: Sea-surface roughness and drag coefficient as function of neutral wind speed. ECMWF Tech. Memo. 630, 8 pp., https://doi.org/10.21957/hcgkicamg.

Hlywiak, J., and D. S. Nolan, 2021: The response of the near-surface tropical cyclone wind field to inland surface roughness length and soil moisture content during and after landfall. *J. Atmos. Sci.*, **78**, 983–1000, https://doi.org/10.1175/JAS-D-20-0211.1.

——, and ——, 2022: The evolution of asymmetries in the tropical cyclone boundary layer wind field during landfall. *Mon. Wea. Rev.*, **150**, 529–549, https://doi.org/10.1175/MWR-D-21-0191.1.

Holland, G. J., 1980: An analytic model of the wind and pressure profiles in hurricanes. *Mon. Wea. Rev.*, **108**, 1212–1218, https://doi.org/10.1175/1520-0493(1980)108<1212:AAMOTW>2.0.CO;2.

Irish, J. L., D. T. Resio, and J. J. Ratcliff, 2008: The influence of storm size on hurricane surge. *J. Phys. Oceanogr.*, **38**, 2003–2013, https://doi.org/10.1175/2008JPO3727.1.

Jing, R., and N. Lin, 2019: Tropical cyclone intensity evolution modeled as a dependent hidden Markov process. *J. Climate*, **32**, 7837–7855, https://doi.org/10.1175/JCLI-D-19-0027.1.

Khairoutdinov, M. F., and K. A. Emanuel, 2013: Rotating radiative-convective equilibrium simulated by a cloud-resolving model. *J. Adv. Model. Earth Syst.*, **5**, 816–825, https://doi.org/10.1002/2013MS000253.

Klotzbach, P. J., D. R. Chavas, M. M. Bell, S. G. Bowen, E. J. Gibney, and C. J. Schreck III, 2022: Characterizing continental US hurricane risk: Which intensity metric is best? *J. Geophys. Res. Atmos.*, **127**, e2022JD037030, https://doi.org/10.1029/2022JD037030.

Knapp, K. R., M. C. Kruk, D. H. Levinson, H. J. Diamond, and C. J. Neumann, 2010: The International Best Track Archive for Climate Stewardship (IBTrACS): Unifying tropical cyclone best track data. *Bull. Amer. Meteor. Soc.*, **91**, 363–376, https://doi.org/10.1175/2009BAMS2755.1.

Lilly, D. K., and K. Emanuel, 1985: A steady-state hurricane model. *16th Conf. on Hurricanes and Tropical Meteorology*, Houston, TX, Amer. Meteor. Soc., 142–143.

Lin, J., K. Emanuel, and J. L. Vigh, 2020: Forecasts of hurricanes using large-ensemble outputs. *Wea. Forecasting*, **35**, 1713–1731, https://doi.org/10.1175/WAF-D-19-0255.1.

Lu, K.-Y., and D. R. Chavas, 2022: Tropical cyclone size is strongly limited by the Rhines scale: Experiments with a barotropic model. *J. Atmos. Sci.*, **79**, 2109–2124, https://doi.org/10.1175/JAS-D-21-0224.1.

Lu, P., N. Lin, K. A. Emanuel, D. Chavas, and J. Smith, 2018: Assessing hurricane rainfall mechanisms using a physics-based model: Hurricanes Isabel (2003) and Irene (2011). *J. Atmos. Sci.*, **75**, 2337–2358, https://doi.org/10.1175/JAS-D-17-0264.1.

Martinez, J., C. C. Nam, and M. M. Bell, 2020: On the contributions of incipient vortex circulation and environmental moisture to tropical cyclone expansion. *J. Geophys. Res. Atmos.*, **125**, e2020JD033324, https://doi.org/10.1029/2020JD033324.

McCartney, G., T. Hacker, and B. Yang, 2014: Empowering faculty: A campus cyberinfrastructure strategy for research communities. *EDUCAUSE Review*, https://er.educause.edu/articles/2014/7/empowering-faculty-a-campus-cyberinfrastructure-strategy-for-research-communities.

Mendelsohn, R., K. A. Emanuel, S. Chonabayashi, and L. Bakkensen, 2012: The impact of climate change on global tropical cyclone damages. *Nat. Climate Change*, **2**, 205–209, https://doi.org/10.1038/nclimate1357.

Merrill, R. T., 1984: A comparison of large and small tropical cyclones. *Mon. Wea. Rev.*, **112**, 1408–1418, https://doi.org/10.1175/1520-0493(1984)112<1408:ACOLAS>2.0.CO;2.

Montgomery, M. T., H. D. Snell, and Z. Yang, 2001: Axisymmetric spindown dynamics of hurricane-like vortices. *J. Atmos. Sci.*, **58**, 421–435, https://doi.org/10.1175/1520-0469(2001)058<0421:ASDOHL>2.0.CO;2.

NHC, 2022: National Hurricane Center tropical cyclone text product descriptions. NOAA, https://www.nhc.noaa.gov/aboutnhcprod.shtml.

Paredes, M., and B. A. Schenkel, 2020: Assessing the role of tropical cyclone size in tornado production. *100th Annual Meeting*, Boston, MA, Amer. Meteor. Soc., S243, https://ams.confex.com/ams/2020Annual/meetingapp.cgi/Paper/371430.

Rotunno, R., and K. A. Emanuel, 1987: An air–sea interaction theory for tropical cyclones. Part II: Evolutionary study using a nonhydrostatic numerical model. *J. Atmos. Sci.*, **44**, 542–561, https://doi.org/10.1175/1520-0469(1987)044<0542:AAITFT>2.0.CO;2.

Shea, D. J., and W. M. Gray, 1973: The hurricane's inner core region. I. Symmetric and asymmetric structure. *J. Atmos. Sci.*, **30**, 1544–1564, https://doi.org/10.1175/1520-0469(1973)030<1544:THICRI>2.0.CO;2.

Tang, B., and K. Emanuel, 2012: A ventilation index for tropical cyclones. *Bull. Amer. Meteor. Soc.*, **93**, 1901–1912, https://doi.org/10.1175/BAMS-D-11-00165.1.

Wang, D., Y. Lin, and D. R. Chavas, 2022: Tropical cyclone potential size. *J. Atmos. Sci.*, **79**, 3001–3025, https://doi.org/10.1175/JAS-D-21-0325.1.

Wang, S., N. Lin, and A. Gori, 2022: Investigation of tropical cyclone wind models with application to storm tide simulations. *J. Geophys. Res. Atmos.*, **127**, e2021JD036359, https://doi.org/10.1029/2021JD036359.

Unauthenticated | Downloaded 07/11/23 03:06 AM UTC

Willoughby, H. E., and M. E. Rahn, 2004: Parametric representation of the primary hurricane vortex. Part I: Observations and evaluation of the Holland (1980) model. *Mon. Wea. Rev.*, **132**, 3033–3048, https://doi.org/10.1175/MWR2831.1.

Xi, D., and N. Lin, 2022: Understanding uncertainties in tropical cyclone rainfall hazard uncertainties using synthetic storms. *J. Hydrometeor.*, **23**, 925–946, https://doi.org/10.1175/JHM-D-21-0208.1.

——, ——, and J. Smith, 2020: Evaluation of a physics-based tropical cyclone rainfall model for risk assessment. *J. Hydrometeor.*, **21**, 2197–2218, https://doi.org/10.1175/JHM-D-20-0035.1.

Xu, J., and Y. Wang, 2010: Sensitivity of tropical cyclone inner-core size and intensity to the radial distribution of surface entropy flux. *J. Atmos. Sci.*, **67**, 1831–1852, https://doi.org/10.1175/2010JAS3387.1.

Zhai, A. R., and J. H. Jiang, 2014: Dependence of US hurricane economic loss on maximum wind speed and storm size. *Environ. Res. Lett.*, **9**, 064019, https://doi.org/10.1088/1748-9326/9/6/064019.

Zhou, W., I. M. Held, and S. T. Garner, 2014: Parameter study of tropical cyclones in rotating radiative–convective equilibrium with column physics and resolution of a 25-km GCM. *J. Atmos. Sci.*, **71**, 1058–1069, https://doi.org/10.1175/JAS-D-13-0190.1.

——, ——, and ——, 2017: Tropical cyclones in rotating radiative–convective equilibrium with coupled SST. *J. Atmos. Sci.*, **74**, 879–892, https://doi.org/10.1175/JAS-D-16-0195.1.

Unauthenticated | Downloaded 07/11/23 03:06 AM UTC